Quantum irreversibility of quasistatic protocols for finite-size quantized systems

Yehoshua Winsten and Doron Cohen
Department of Physics, Ben-Gurion University of the Negev, Beer-Sheva 84105, Israel

Quantum mechanically, a driving process is expected to be reversible in the quasistatic limit, also known as the adiabatic theorem. This statement stands in opposition to classical mechanics, where a mix of regular and chaotic dynamics implies irreversibility. A paradigm for demonstrating the signatures of chaos in quantum irreversibility is a sweep process whose objective is to transfer condensed bosons from a source orbital. We show that such a protocol is dominated by an interplay of adiabatic-shuttling and chaos-assisted depletion processes. The latter is implied by interaction terms that spoil the Bogoliubov integrability of the Hamiltonian. As the sweep rate is lowered, a crossover to a regime that is dominated by quantum fluctuations is encountered, featuring a breakdown of quantum-to-classical correspondence. The major aspects of this picture are not captured by the common two-orbital approximation, which implies failure of the familiar many-body Landau-Zener paradigm.

I. INTRODUCTION

In classical mechanics, contrary to a prevailing misconception, the quasistatic limit is in general *not* adiabatic. This observation implies that protocols become irreversible, even if their control parameters are varied very very slowly. Adiabaticity and reversibility in the quasistatic limit are guaranteed only if the phase space of the system does not undergo structural changes. Accordingly, one distinguishes between the integrable-dynamics version of adiabaticity [1], where action integrals serve as adiabatic invariants, and the chaotic-dynamics version of adiabaticity [2–8], where the phase-space volume is the adiabatic invariant. Generic systems feature *mixed phase space* that contains both quasiregular and chaotic dynamics. Such systems do not obey the standard adiabatic theorems. The simplest demonstration for such irreversibility is the *separatrix crossing* scenario that has been discussed extensively in the mathematical literature [9–19]. But generic systems have more than a single degree of freedom, and therefore chaos becomes a central theme in the analysis [20–24].

In this paper we would like to explore how the above picture is reflected or modified *in the quantum framework*. The most suitable arena for such studies concerns the dynamics of condensed bosons. In order to avoid an abstract discussion, let us consider a specific generic scenario. Let us assume that initially the bosons are condensed in a source orbital. A sweep protocol is designed to transfer them to a different orbital. *Naively*, one is inclined to speculate that this would be merely a many-body version of the Landau-Zener (LZ) adiabatic passage problem. The classical limit, also known as the nonlinear LZ problem, has been studied extensively [25,26]. It features a *diabatic ejection* stage (Fig. 1, left panel) that is related to a swallow-tail structure in its bifurcation diagram. The full quantum version has been addressed as well [27]. Irreversibility has not been discussed there, but it is expected due to the separatrix crossing, per the conditions of the Kruskal-Neishtadt-Henrard theorem [9–19].

We claim that in general the many-body LZ problem cannot serve as a paradigm for depletion. Typically the dynamics involves more than two orbitals, meaning that we are dealing with more than one degree of freedom. Consequently the role of *chaos* cannot be ignored [22–24]. Using different phrasing, we say that the inapplicability of the LZ paradigm is related to the failure of the two-orbital approximation (TOA). Once additional orbitals are taken into account, the integrability of the Hamiltonian is spoiled. Consequently, the depletion stage involves competing mechanisms which we call *adiabatic shuttling* and *chaos-assisted depletion* (Fig. 1, middle and right panels).

Our interest is to address the *irreversibility* theme, and to contrast *quantum* against *semiclassical* dynamics. In our semantics the term "semiclassical" replaces the term "classical" whenever the quantum state is represented in phase space by a cloud of points, that are propagated using classical equations of motion. This is also known as the "truncated Wigner approximation," and goes much beyond the single-trajectory dynamics of mean-field theory. Nevertheless, semiclassical approximation, in this restricted sense, is not capable of taking into account either tunneling [28–31] or interference of separated trajectories.

In quantum mechanics, contrary to the semiclassical picture, the quasistatic limit of a closed finite system is always adiabatic, and therefore reversible. This is because the energies are quantized, and therefore the system follows the (gapped) ground state for slow enough driving. However, this quantum adiabaticity has no experimental significance once we deal with a mesoscopic system. In the example that we discuss in this paper, the condensate is a flow state of a superfluid ring. As the control parameter is varied, the flow state becomes *metastable*. But the tunnel coupling to the new ground state is exponentially small in the number of particles [28], and therefore can be ignored. Hence the system fails to follow the ground state. This is in fact the essence of superfluidity. The question remains: What is the fate of the flow state as the control parameter is further varied? What is the
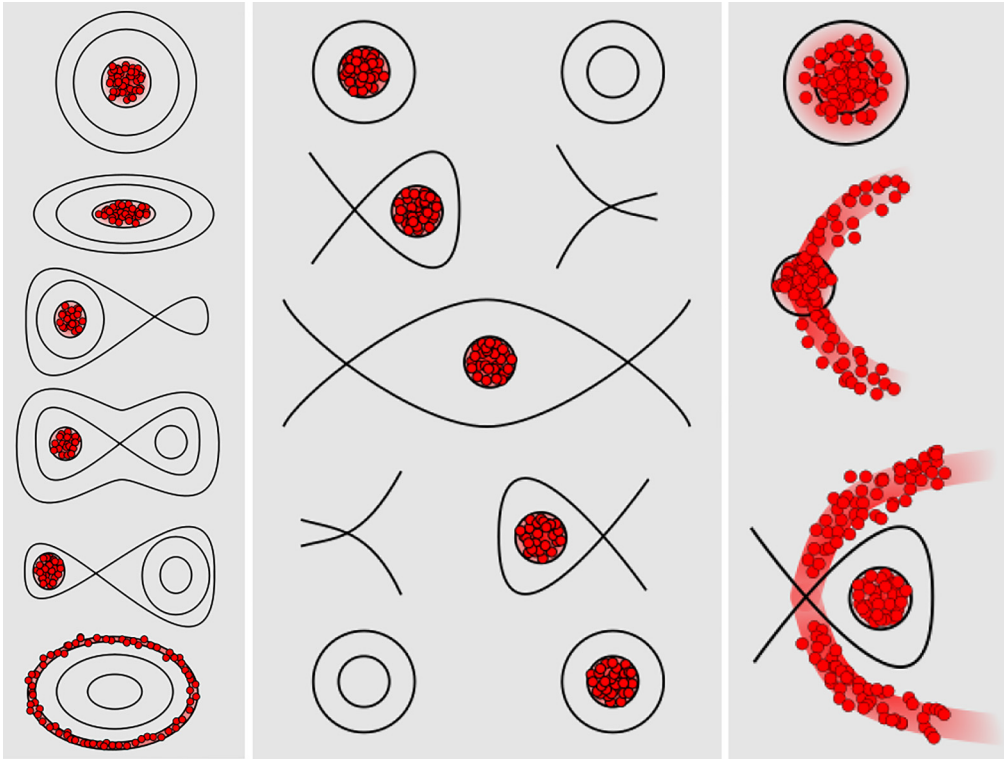
FIG. 1. Schematics of phase-space evolution. Each panel provides a sequence of phase-space snapshots. In the left and middle panels the curves are $\mathcal{H} = \text{const}$ contours of a one-degree-freedom system. The evolving cloud is red. Initially the cloud is located in the minimum of the energy landscape. The left panel displays an *adiabatic shuttling* process. As a control parameter is varied a second local minimum appears due to a saddle-node bifurcation (third snapshot), and the cloud becomes metastable (fifth snapshot). In a quantum perspective the evolution is *diabatic*, meaning that quantum tunneling does not have the time to take place. The process ends with *diabatic ejection* (last snapshot). If the sweep is reversed (not shown), the cloud can *split* into the two minima of the fifth snapshot (assuming that both basins are expanding). The middle panel displays a *relay-shuttling* process. It consists of pitchfork bifurcation, swap of separatrices, and inverse pitchfork bifurcation. The right panel displays the effect of a *chaos-assisted depletion* mechanism that competes with the pitchfork bifurcation of the relay-shuttling process. Strictly speaking we display in this panel a Poincaré section of a two-degree-of-freedom system. Due to spoiled integrability, there is a chaotic strip along which spreading is allowed. The outer part of the cloud starts to spread away before the central fixed point becomes unstable.

mechanism of depletion? Do we have the same irreversibility as in the semiclassical analysis?

The question that we pose is not merely related to the foundations of physics (irreversibility, quantum vs classical). It is also of practical importance for the design of protocols whose objective is to manipulate many-body states of cold atoms, also known as atomtronics [32]. Specifically, we consider bosons that are described by the Bose-Hubbard Hamiltonian (BHH). This model is of major interest both theoretically and experimentally [33–36]. There is a particular interest in lattice-ring circuits that can serve as a superconducting quantum interference device (SQUID) or as a useful qubit device [37–40]. The hope is to achieve coherent operation for BHH configurations that involve a few orbitals. This is the natural extension of studies that concern two orbitals, also known as the bosonic Josephson junction. The most promising configuration is naturally the three-site trimer [41–59]. For the analysis of such circuits one has to confront the handling of an underlying mixed phase space [57,58,60].

We are inspired by hysteresis experiments, as done for double-well geometry [61], and by protocols that have been realized experimentally for bosons in a ring (or SQUID) geometry [32,62–65]. The related theoretical studies adopt the TOA, and highlight the appearance of swallow-tail bifurcations [66–70]. But the failure of the TOA is anticipated by observing that the Bogoliubov pairing interaction requires three orbitals, and by the further observation that there are additional terms in the Hamiltonian that spoil the integrability of the Bogoliubov approximation. Consequently, our interest below is to push the discussion of irreversibility into the realm of high-dimensional dynamics, addressing the fingerprints of chaos and mixed phase space in the quantum-mechanical reality.

The classical analysis of the forward sweep process follows our previous publication [24]. In the present paper we further illuminate that the integrable mechanism that is implied by the Bogoliubov approximation is a variant of adiabatic shuttling that we call *relay shuttling* (Fig. 1). In the quasistatic limit this mechanism is overwhelmed by chaos-assisted depletion. We explore the *quantum* scenario, and append an *inverse sweep* of the control parameter, in order to study the *irreversibility* due to the interplay of the various mechanisms involved. Our major observation is the discovery of a regime of *quantum irreversibility*, that has not been anticipated by the

semiclassical analysis of [24]. This regime features *universal quantum fluctuation* (UQF), and an unexpected breakdown of *quantum-to-classical correspondence* (QCC).

Outline

We present the Bose-Hubbard Hamiltonian that describes a superfluid ring, and display some results of simulations that probe irreversibility. The protocol for a proposed experiment with an atomtronic circuit is highlighted: a superfluid ring whose rotation velocity is gradually increased and then decreased back to zero. We illuminate our findings by performing step-by step analysis: We clarify the failure of the TOA; we provide predictions that are based on the Bogoliubov approximation; and then, going beyond that, we discuss the implications of chaos. This is followed by a discussion, where we highlight the manifestation of UQF and the breakdown of QCC.

II. THE MODEL

Consider N bosons in an L-site ring, described by the BHH with hopping frequency K and on-site interaction U. The sweep control parameter is the Sagnac phase Φ, which is proportional to the rotation velocity Ω of the device. This phase can be regarded as the Aharonov-Bohm flux that is associated with a Coriolis field in the rotating frame. The Hamiltonian is

$$\mathcal{H} = \sum_{j=0}^{L-1} \left[\epsilon_j a_j^\dagger a_j + \frac{U}{2}(a_j^\dagger a_j^\dagger a_j a_j) \right.$$
$$\left. - \frac{K}{2}\left(e^{i\frac{\Phi}{L}}a_{j+1}^\dagger a_j + e^{-i\frac{\Phi}{L}}a_j^\dagger a_{j+1}\right) \right] \quad (1)$$

where $\epsilon_j = -\epsilon \cos(2\pi j/L)$ is included, as in [69]. It signifies an external gravitation potential that may arise due to an optional *tilt* of the ring. Some optional representations of the Hamiltonian are presented in Appendixes A and B. Unless stated otherwise we assume $\epsilon = 0$. The notation $u = NU/K$ stands for the dimensionless interaction strength, and in the numerical simulations we use units of time such that $K = 1$.

The momentum orbitals are labeled by the wave number $k = (2\pi/L) \times$ integer, where the integer is the winding number. In this basis the Hamiltonian takes the form

$$\mathcal{H} = \sum_{k=0}^{L-1} \mathcal{E}_k b_k^\dagger b_k \; - \; \frac{\epsilon}{2}\sum_{k,\pm} b_{k\pm1}^\dagger b_k + \frac{U}{2L} \sum_{k_1,k_2,k_3,k_4}' b_{k_1}^\dagger b_{k_2}^\dagger b_{k_3} b_{k_4} \quad (2)$$

where the prime in the k summation implies that conservation of total momentum is required. The presence of the control parameter Φ is implicit via

$$\mathcal{E}_k = -K\cos\left(k - \frac{\Phi}{L}\right). \quad (3)$$

A. Preparation

We start with a nonrotating ring ($\Phi = 0$). Initially the bosons are condensed in the zero-momentum orbital ($k_0 = 0$). Keeping only the three lowest orbitals, labeled as (k_0, k_+, k_-),
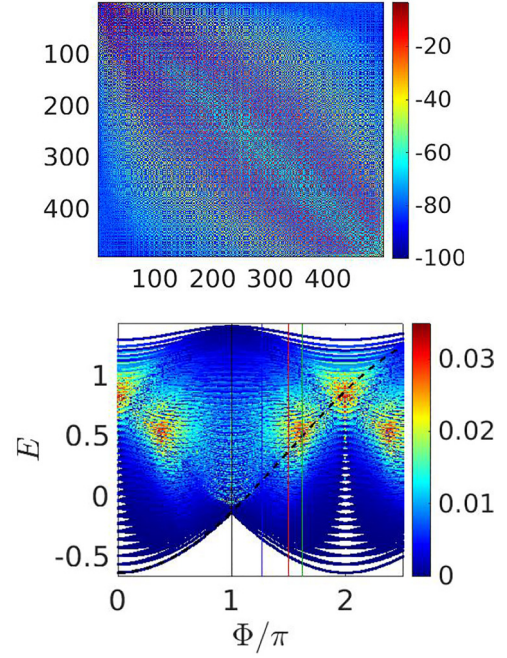

FIG. 2. Signatures of quantum chaos. We consider a trimer with $N = 30$ particles. The upper panel is an image of the matrix $|I_{\nu,\mu}|^2$, color coded in log scale. The model parameters are $K = 1$ and $u = 2.3$ and $\Phi = 1.6\pi$. From this matrix we extract the chaoticity measure s_ν for each energy level. The lower panel shows the energy levels $E_\nu(\Phi)$ as a function of $\Phi \in [0, 2.5\pi]$. The levels are color coded by s. The black line indicates the energy of the $k = 0$ condensate, if it is not depleted. The vertical lines are the thresholds $\Phi_{\text{mts}} = 1\pi$ (black), $\Phi_{\text{stb}} = 1.26\pi$ (blue), $\Phi_{\text{dyn}} = 1.5\pi$ (red), and $\Phi_{\text{swp}} = 1.62\pi$ (green). Later we we shall see that in a sweep process a depletion process takes place during the time that Φ crosses these thresholds.

it is convenient to describe their subsequent occupation using the depletion coordinate n, and the imbalance coordinate M, that are defined as follows:

$$n = \sum_{k\neq0} n_k = n_+ + n_-, \quad (4)$$
$$M = n_+ - n_-. \quad (5)$$

B. Quantum chaos

One can regard the BHH as the Hamiltonian of coupled nonlinear oscillators. Standard analysis reveals that the underlying classical phase space is a mix of chaotic and quasiregular regions. This may have signatures both in the many-body eigenstates that are labeled using a running index ν, and in the statistics of the associated eigenenergies E_ν. Respectively, one can characterize the spectrum using "quantum chaos" measures s and r (see Appendix C). Such a type of characterization has been illustrated, e.g., in Fig. 1 of [71] for a trimer chain. A more refined version of s, and discussion of its L dependence, has been provided in [72].

In the present context the r indicator is not useful, because we have mixed phase space, and the chaotic region of interest is rather small. In contrast, the s indicator is informative. Figure 2 provides an illustration of the matrix $I_{\nu,\mu} = \langle \nu|(-\partial\mathcal{H}/\partial\Phi)|\mu\rangle$. The band profile of this matrix is related to the correlator of the current operator $I(t)$. The

quantum chaos indicator s_ν is extracted from this matrix for each energy level. A second panel displays the variation of the energy levels versus the control parameter Φ. The levels are color coded by s. Vertical lines indicate the thresholds Φ_{mts} (black), Φ_{stb} (blue), Φ_{dyn} (red), and Φ_{swp} (green). The first threshold Φ_{mts} is positioned where the k_+ orbital crosses the k_0 orbital and becomes the lowest in energy. The other thresholds will be defined in later sections; namely, at Φ_{stb} the Landau stability is lost, at Φ_{dyn} dynamical stability is lost, and at Φ_{swp} we have a swap of separatrices that is related to the relay-shuttling mechanism.

III. PROBING IRREVERSIBILITY USING AN ATOMTRONIC CIRCUIT

A. The proposed experimental setup

Consider a ring with condensed bosons. The optical potential that holds the bosons is possibly painted as in [64]. The ring has several weak links (as in SQUID geometry), or it can be an L-site lattice ring (as assumed below). Initially the ring is at rest, and the condensed bosons have zero momentum. In a *quench* protocol the ring starts abruptly to rotate. Superfluidity means that the rotation velocity Ω should be larger than a critical value Ω_c in order to induce current. The appearance of a nonzero current (depletion of the zero-momentum orbital) can be verified using a standard time-of-flight measurement procedure. We would like to consider a *sweep* protocol, such that the rotation velocity is increased gradually (quasistatically) from zero to a finite value that is larger than Ω_c. Then we ask whether this sweep process is reversible. Accordingly, we decrease gradually Ω back to zero. Our main message, from the perspective of an experiment, is that the quasistatic protocol features *quantum irreversibility*. A secondary message is that the value of Ω_c is affected by the sweep rate, and provides an indication for the underlying depletion mechanism.

B. Results of numerical simulations

We present some results of numerical simulation for an $L = 3$ ring, also known as a trimer. This will motivate the analysis in the subsequent sections. Initially all the particles are condensed in $k = 0$, meaning that the initial value of the depletion coordinate is $n = 0$. The protocol consists of three stages: a forward sweep of Φ from $\Phi = 0$ to 2.5π, an optional waiting period, and a backward sweep to $\Phi = 0$. Note that once Φ exceeds $\Phi_{\text{mts}} = \pi$ (to be indicated by the black vertical line in the time axis of our figures) the condensate becomes metastable. But its depletion happens only in a later stage, as discussed below.

We display in Fig. 3 the variation of (E, n) as a function of time using both quantum and semiclassical simulations. The variation of n is color coded. In the semiclassical simulations we propagate an ensemble of trajectories, starting with a cloud that mimics the initial condensate. In the quantum simulations we propagate the evolving many-body state $\Psi(t)$, and calculate the probabilities

$$p_\nu(t) = |\langle E_\nu | \Psi(t) \rangle|^2. \tag{6}$$

The energy levels $E_\nu[\Phi(t)]$ are plotted as a function of time: gray color indicates levels whose weight is vanishingly small
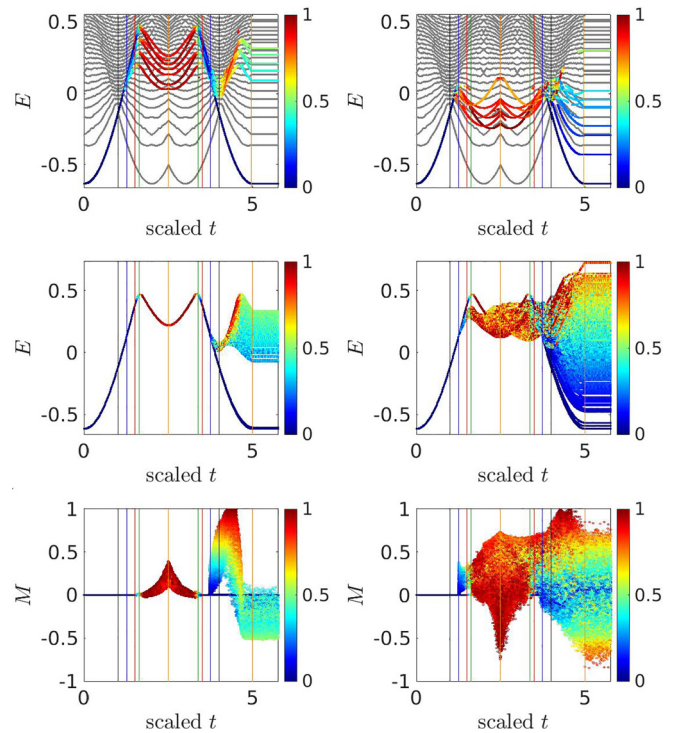

FIG. 3. Simulations that test irreversibility. The control parameter is swept from $\Phi = 0$ to 2.5π and back to $\Phi = 0$. The horizontal axis is the scaled time $(1/\pi)|\dot{\Phi}|t$. The vertical lines are as in Fig. 2. The two additional orange lines indicate where the sweep is reversed ($\Phi = 2.5\pi$) and stopped (back at $\Phi = 0$). Note that the quantum simulations may include an additional waiting period at $\Phi = 2.5\pi$. The initial state is the ground-state condensate. The upper panels are quantum simulation for $N = 30$ particles, with $K = 1$ and $u = 2.3$. The energy levels $E_\nu[\Phi(t)]$ are plotted. Gray color indicates levels whose weight p_ν is vanishingly small (for presentation purposes this set is diluted by factor 10). The participation levels whose p_ν is non-negligible are color coded by $\langle n \rangle_\nu$. The left panel is for $\dot{\Phi} = 5\pi \times 10^{-4}$, and the right panel is for $\dot{\Phi} = 3.33\pi \times 10^{-7}$. The second and third rows display semiclassical simulations for the same system. We plot E and M for an ensemble of trajectories, starting with a cloud that mimics the initial condensate. The value of the n coordinate is color coded. The left panel is for a slow sweep $\dot{\Phi} = 5\pi \times 10^{-4}$, while the right is for a *very* slow sweep $\dot{\Phi} = 5\pi \times 10^{-5}$. In this figure, and in all subsequent figures, the units are normalized ($n := n/N, M := M/N, E := E/N$).

(less than 3.5%), and the other levels whose p_ν is non-negligible are color coded by $\langle n \rangle_\nu = \langle E_\nu | n | E_\nu \rangle$.

One observes that for "slow" sweep the spreading in E is worse, indicating that irreversibility is enhanced. For the semiclassical simulation we show in Fig. 3 (third row) how this spreading is expressed in M. The optional Fig. 9 of Appendix D shows what the spreading looks like in occupation space, using (n, M) coordinates.

In Fig. 4 we plot the depletion $\langle n \rangle$ versus time. In the quasistatic regime the time of the depletion t_d is determined by inspection of the sharp rise in $\langle n \rangle$. We indicate by dark gray background color the range of $\dot{\Phi}$ where t_d becomes ill defined, reflecting a lag with respect to the parametric variation of Φ. In the quasistatic regime we observe that $\Phi(t_d)$ is shifted as $\dot{\Phi}$
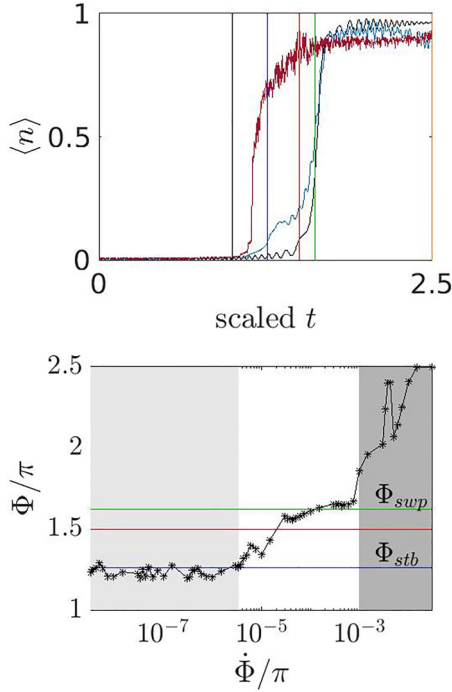
FIG. 4. Depletion vs sweep rate. The upper panel displays the depletion $\langle n \rangle$ vs time for a quantum simulation with sweep rate $\dot\Phi = 5\pi \times 10^{-4}$ (blue) and with very slow rate $\dot\Phi = 3.33\pi \times 10^{-7}$ (red). The former is compared with simulation (black) that is generated by the Bogoliubov-approximated Hamiltonian. The vertical lines and the parameters are as in Fig. 3. From such plots we determine the time t_d at which the depletion happens. The dependence of $\Phi(t_d)$ on the sweep rate $\dot\Phi$ is displayed in the lower panel. The dark gray background indicates the nonquasistatic regime where the depletion time lags and becomes numerically ill defined. In the quasistatic regime the observed dependence on $\dot\Phi$ indicates the crossover from chaos-assisted depletion (light gray background) to adiabatic shuttling. Namely, the depletion shifts from Φ_{stb} to Φ_{swp}.

is increased. Later we interpret this shift as an indication for a crossover from chaos-assisted depletion to adiabatic shuttling.

In order to quantify the *adiabaticity* in the quantum simulations, we characterize the spreading in energy by estimating the number of participating energy levels:

$$N_{\text{states}}(t) = \left[\sum_\nu |p_\nu(t)|^2 \right]^{-1}. \tag{7}$$

An optional measure is $N_{\text{orbitals}}(t)$ of Appendix E. Illustrations for the temporal variation of both measures are provided in Appendix F. It should be noted that $N_{\text{states}}(t)$ is expected to be monotonic increasing only for a strictly quasistatic process, which is not the case here (because we have mixed phase space and bifurcations along the way). Nevertheless, the final spreading can be used as a measure for the *irreversibility* of the sweep protocol. Its dependence on the rate $\dot\Phi$ is displayed in Fig. 5.

We see that in the quasistatic regime slowness is bad for adiabaticity. This is very pronounced in the semiclassical simulation, and has modest reflection in the quantum evolution. On the average, irreversibility is suppressed quantum
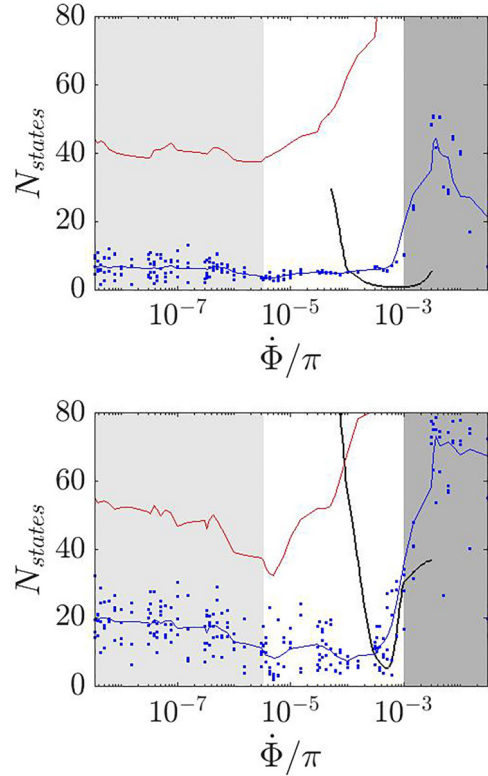

FIG. 5. Irreversibility vs sweep rate. Irreversibility is indicated by the growth of the the number N_{states} of energy levels that participate in the evolution. We show the dependence of N_{states} (blue dots) on the sweep rate $\dot\Phi$ before the reversed sweep (upper panel) and at the end of the reversed sweep (lower panel), for miscellaneous values of the waiting time. The erratic dependence on the waiting is illustrated in Fig. 12 of Appendix F. The blue lines provides the average value of N_{states}, and the red lines provided the average value $\sum \nu p_\nu$. The black lines are based on the semiclassical simulations. The gray background is the same as in Fig. 4.

mechanically compared with the semiclassical expectation. But more interestingly, the dependence of N_{states} on $\dot\Phi$ becomes erratic, indicating a crossover to a regime of chaos-assisted-depletion. This crossover is further reflected in the timing of the depletion, as we already saw in Fig. 4.

IV. COMMON APPROXIMATIONS THAT EXCLUDE "CHAOS"

A. Two orbital approximation

As we sweep the parameter Φ, orbitals k_0 and k_+ cross each other. It is therefore natural to adopt TOA as in [69]. This naturally leads to an effective two-site (dimer) problem as in [27], that can be regarded as a second-quantized version of the well-known nonlinear LZ problem [25,26].

With TOA, the third term in Eq. (2) does not generate transitions between orbitals. Therefore we need a tilt $\epsilon \neq 0$ in order to get nontrivial dynamics. Indeed this was the approach in [69]. But clearly for a BHH ring we should have nontrivial dynamics even without a tilt. So clearly TOA is an oversimplification. Nevertheless one may wonder whether with $\epsilon \neq 0$
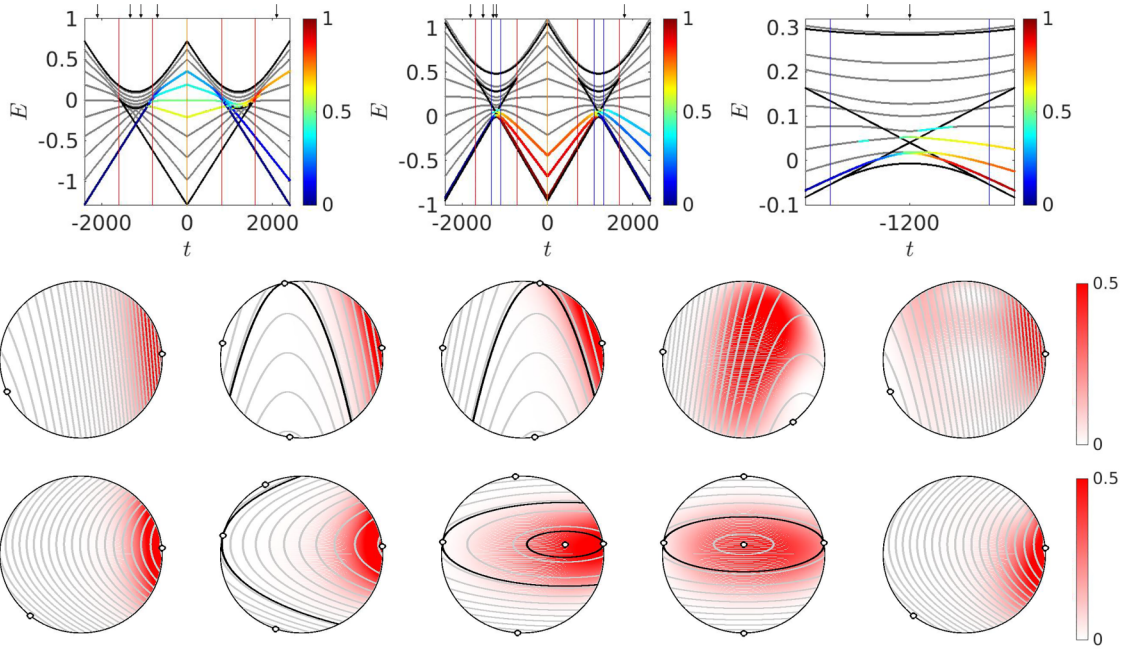
FIG. 6. Quantum simulations for the dimer. We consider $N = 10$ particles whose dynamics is generated by the Hamiltonian Eq. (8). The upper panels are for diabatic ejection scenario (left), relay shuttling (middle), and zoom of the latter (right). The units of time are such that $K = 1$, and the tilt is $\epsilon = 0.2$. The interaction parameters are given respectively by Eq. (9) with $u = 3.45$ and by Eq. (10) with $u = 2.3$, with $L = 3$. The sweep is from $\mathcal{E} = 2$ to -2 and back to $\mathcal{E} = 2$, with rate $\dot{\mathcal{E}} = 1/600$. Energy levels E_ν are plotted vs time. Levels whose p_ν is vanishingly small are in gray. The other levels are color coded by $\langle n \rangle_\nu$. The energies of the minima, maxima, and separatrices are indicated by black lines. Bifurcation points are indicated by vertical lines. Snapshots of the evolution are taken at times that are indicated by small black arrows, and placed at the second row (diabatic ejection) and at the third row (relay shuttling). At each snapshot we plot the Husimi representation Eq. (E3) (red is high intensity) of the quantum state, using (S_x, S_z) phase-space coordinates. We overplot energy contours of the Hamiltonian, and indicate in black the extremal points and the separatrices.

there is a regime such that TOA makes sense. We address this secondary question in Appendix G.

B. Bogoliubov approximation

The Bogoliubov approximation keeps in Eq. (2) transitions of *pairs* from the k_0 condensate to the $k_\pm$ orbitals. The textbook version further makes the substitution $b_0 \mapsto \sqrt{N}$, but we avoid below this oversimplification. Either way, it is clear that the Bogoliubov approximation implies that in the absence of tilt ($\epsilon = 0$) the occupation imbalance (M) is a constant of motion. Consequently, for the $L = 3$ trimer (or for any ring if we keep the three lowest orbitals $k_0, k_+,$ and k_-) the BHH becomes formally identical to a generalized dimer Hamiltonian, that differs from the standard TOA dimer.

We present the derivation of the effective $\mathcal{H}_{\mathrm{dimer}}$ in Appendix A, and further discuss it below. The same $\mathcal{H}_{\mathrm{dimer}}$ can be exploited to simulated the TOA dynamics using an appropriate set of effective parameters, and to simulate the Bogoliubov dynamics using a different set of effective parameters. The dynamics that is generated in the two cases is illustrated in Fig. 6. One observes that the TOA dynamics (with tilt) features *diabatic ejection*. As opposed to that, the Bogoliubov-approximated dynamics features what we call *relay shuttling*. The snapshots of the evolution that are provided in Fig. 6 correspond to the scenarios that have been illustrated in Fig. 1.

Coming back to Fig. 4 we observe that the t_d of the Bogoliubov (black) line agrees with that of the blue line, but not with

that of the red line. This implies that in the latter case (very slow sweep) the depletion mechanism is *not* a relay-shuttling process.

C. The generalized dimer problem

Both the TOA (with tilt) and the Bogoliubov approximation (with or without tilt) lead to an effective dimer problem. See Appendixes A and G. The dimer Hamiltonian can be written using generators of spin rotations. Namely, S_z is defined as half the occupation difference in the site representation, while $S_x = (n_0 - n_1)/2 = (N/2) - n$ is half the occupation difference in the momentum orbital representation. Thus, S_x is merely a shifted version of the depletion coordinate. What we call the generalized dimer Hamiltonian contains two distinct interaction terms:

$$\mathcal{H}_{\mathrm{dimer}} = -\mathcal{E}S_x - \epsilon S_z + U_\parallel S_z^2 + U_\perp S_x^2. \quad (8)$$

In Appendix B we show that the TOA reduces to this form with

$$U_\parallel = 0, \qquad U_\perp = -\frac{1}{L}U \qquad \text{[TOA]}. \quad (9)$$

In contrast, the Bogoliubov approximation features, due to the pairing interaction,

$$U_\parallel = \frac{2}{L}U, \qquad U_\perp = \frac{1}{4L}U \qquad \text{[Bogoliubov]}. \quad (10)$$
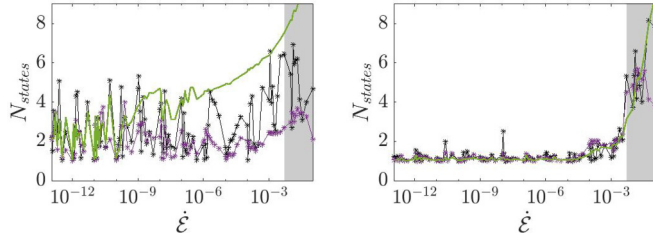
FIG. 7. Irreversibility vs sweep rate for the dimer. For simulations as in Fig. 6, we plot N_{states} vs the sweep rate $\dot{\mathcal{E}}$ at the end of the forward sweep (purple), and at the end of the reversed sweep (black). The left panel is for the diabatic ejection scenario, and the right panel is for the relay shuttling scenario. Additionally we plot (in green) the average level index at the end of the forward sweep. The nonquasistatic region (gray) is determined by inspection of the $N_{orbitals}$ plot of Appendix F.

The detuning parameter $\mathcal{E}$ reflects the excitation energy of the condensate. For the TOA it is $\mathcal{E} = \mathcal{E}_+ - \mathcal{E}_0$, while for Bogoliubov it is

$$\mathcal{E}(\Phi) = \frac{1}{2}(\mathcal{E}_+ + \mathcal{E}_-) - \mathcal{E}_0 + \frac{NU}{4L}. \tag{11}$$

As Φ is increased, $\mathcal{E}$ decreases, and at Φ_{swp} it swaps sign, namely, $\mathcal{E}(\Phi_{swp}) = 0$. The swap location is indicated by the green vertical line in the time axis of our figures.

We further show in Appendix I that the bifurcation scenario depends on the relative magnitudes of the Us. The parameters $U_\perp$ and $U_\parallel$ have the same sign (the latter is zero for TOA). Accordingly, phase-space contours on the Bloch spheres are ellipses (or parabolas) in the (S_x, S_z) coordinates. If we vary the control parameter $\mathcal{E}(\Phi)$, there are two different bifurcation scenarios depending on which interaction is larger. The two scenarios are compared in Figs. 6 and 7, and further discussed below.

Consider the TOA, for which we have $|U_\perp| > |U_\parallel|$. For large $\mathcal{E}$ the lowest energy is in the east pole, which supports condensation in orbital zero. As $\mathcal{E}$ is decreased, a bifurcation appears at the west hemisphere, with a separatrix that move to the east. This leads eventually to a diabatic ejection of the condensed cloud. We show in Appendix I that the pertinent bifurcation happens at

$$\mathcal{E}_c = [(|U_\parallel - U_\perp|N)^{2/3} - \epsilon^{2/3}]^{3/2}. \tag{12}$$

Consider the Bogoliubov approximation, for which we have $|U_\perp| < |U_\parallel|$. Here two bifurcations take place: The first bifurcation appears at the west hemisphere, and is formally the same as that of Eq. (12). The same expression for $\mathcal{E}_c$ applies. However, this bifurcation has no significance, as implied by Fig. 6. It is followed by a second bifurcation of the east pole that for zero tilt is determined by the condition $\mathcal{E}(\Phi) = \mathcal{E}_{dyn}$, where $\mathcal{E}_{dyn} = NU_\perp$. For nonzero tilt we derive in Appendix I the more general expression

$$\mathcal{E}_{dyn} = \left[1 - \left(\frac{\epsilon}{U_\parallel N}\right)^2\right]^{1/2} NU_\perp. \tag{13}$$

This bifurcation signifies the loss of dynamical stability of the condensate (the elliptic fixed point becomes hyperbolic),

and therefore the above condition can be used to determine Φ_{dyn}. Due to the bifurcation a new minimum is born, and a relay-shuttling process is initiated. Subsequently, at Φ_{swp}, there is a swap of separatrices, and consequently, hereafter, the minimum that had bifurcated from the east belongs to the basin of the west. The net effect is relay shuttling from east to west that ends when $\mathcal{E}(\Phi) = -\mathcal{E}_{dyn}$. This scenario is illustrated in Fig. 6.

V. THE MANIFESTATION OF CHAOS

Once we go beyond the Bogoliubov approximation, the imbalance M is no longer a constant of motion. Using action angle variables (n, M, and their conjugates) it is possible to express the three-orbital Hamiltonian as the sum of integrable Bogoliubov term $\mathcal{H}^{(0)}(n, \varphi; M)$ that conserves M and additional terms $\mathcal{H}^{(\pm)}$ that spoil the integrability. See [24] and Appendix B for explicit expressions. The $\mathcal{H}^{(\pm)}$ terms allow slow depletion of the cloud by drifting away from $M = 0$.

Figures 8(a)–8(c) clarify how phase space changes as Φ is varied. It is the inspiration for the illustration in the right panel of Fig. 1. Snapshots are taken after Φ_{mts}, after Φ_{stb}, and after Φ_{dyn}. It shows how the $n = 0$ fixed point changes from metastable minimum to elliptic fixed point and then becomes unstable. We also have an indication for the emerging shuttling island. The small island that we see in the right panel of row (c) is in fact a section of a torus that resides above the captured cloud. The latter can be located in a Poincaré section at a slightly lower energy (not displayed). The chaotic region allows an optional depletion process that we further discuss in the next paragraph.

A necessary condition for chaos-assisted depletion is to have a potential floor that goes down from $n = M = 0$ in the $M \neq 0$ direction. This is the Landau criterion for instability of the superflow. Namely, $n = 0$ becomes a saddle rather than a local minimum in the energy landscape. The Landau instability is encountered once we cross Φ_{stb}, which is indicated by the blue vertical line in the time axis of our figures. Bogoliubov analysis [24] provides the explicit expression

$$\Phi_{stb} = 3 \arccos\left[\frac{1}{6}(\sqrt{u^2 + 9} - u)\right] \tag{14}$$

where $u = NU/K$ is the dimensionless interaction strength. But we have to remember that only later, at Φ_{dyn}, the $n = 0$ location becomes dynamically unstable, as shown in Fig. 8(c). This means that for $\Phi_{stb} < \Phi < \Phi_{dyn}$ only the outer piece of the cloud can drift away from $M = 0$ via the chaotic region. The implied branching is clearly demonstrated in Fig. 3 and optionally in Fig. 9 of Appendix D.

The splitting of the cloud, into an $M = 0$ shuttling branch and $M \neq 0$ chaotic spreading, is responsible for the crossover to chaos-assisted depletion. The latter is a very slow process, and therefore becomes noticeable only for very slow sweep rate. It is clearly distinct from shuttling, because it starts earlier, at Φ_{stb}, unlike the shuttling that starts at Φ_{dyn}.

In the reversed sweep we see once again this branching effect. In fact it is more conspicuous on the way back: the cloud stretches further in the M direction, which becomes possible because the ceiling of the potential is going up, hence not blocking further expansion. An optional way to illustrate this branching is provided by Fig. 9 of Appendix D.
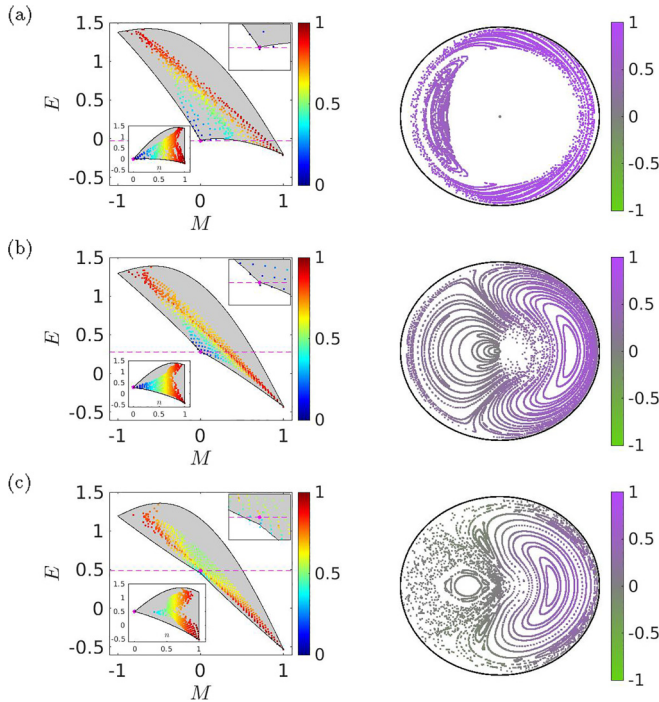
FIG. 8. Mixed chaotic phase space. The energy landscape of the BHH trimer for $u = 2.3$. (a)–(c) $\Phi = 1.1\pi$, 1.4π, and 1.6π, respectively. Respectively they feature energetic stability, dynamical stability, and instability of the condensate. Each point in the left panels represents an eigenstate that is positioned according to its E_ν and $\langle M \rangle_\nu$, and color coded according to its $\langle n \rangle_\nu$. Looking at the classical Hamiltonian $\mathcal{H}(n, \varphi; M, \phi)$, for each M we find the floor (minimum) and the ceiling (maximum) of the energy, and get the black solid lines that bound the spectrum from below and from above. The $n = M = 0$ central fixed point is indicted by a pink dot. Its vicinity is zoomed in the upper inset, and its energy is indicted by a dashed line. For this energy a Poincaré section of phase space is displayed in the right panel, where each section point of a trajectory is color coded by its M, and displayed using its (n, φ) as polar coordinates. (c) $\Phi > \Phi_{\text{dyn}}$, for which the central point is an unstable saddle immersed in chaos. Therefore it cannot support an eigenstate. This observation is better delivered by the lower inset, where the same spectrum is plotted with n serving as horizontal axis.

VI. MECHANISMS FOR IRREVERSIBILITY

In linear-response theory (Kubo formalism), irreversibility is related to accumulated deviation from adiabaticity. It is controlled by the ratio between the sweep rate and the natural frequency of the driven system. This picture assumes that the cloud follows an evolving adiabatic manifold in phase space. In the quasistatic limit, linear-response theory implies reversibility. But this picture breaks down if during the sweep a violent event takes place. In the nonlinear LZ problem the local minimum is diminished at a particular moment of the sweep process due to an inverse saddle-node bifurcation (see Fig. 1), and consequently the cloud is ejected and stretched along the fading separatrix. This is what we call *diabatic ejection*. On the way back the cloud can split between two regions as implied by the Kruskal-Neishtadt-Henrard theorem [9–19]. This type of dynamics is reflected in the quantum dynamics (see Fig. 6 for demonstration).

In the problem under consideration, *diabatic ejection* is an artifact of the TOA. Instead we find that the Bogoliubov approximation predicts *relay shuttling*. A gentle type of irreversibility can arise when the shuttling process starts or ends (pitchfork bifurcations). See Fig. 10 of Appendix F for demonstration. A quantitative comparison of the irreversibility that is associated with the two mechanisms is provided in Fig. 7.

As we already discussed, for very slow sweep a different depletion mechanism takes over, that goes beyond Bogoliubov, namely, chaos-assisted depletion. This mechanism gives rise to "free expansion" of the cloud in phase space (M is not constant of motion). Furthermore, once the sweep is reversed the cloud undergoes a conspicuous branching process, as discussed previously for Figs. 3 and 9. Thus, irreversibility is extremely enhanced in the semiclassical simulations. Quantitatively this has a modest manifestation in the quantum-mechanical case. On the other hand, we observe a regime of quantum irreversibility that exhibits quantum chaos characteristics and breakdown of QCC that we further discuss below.

VII. UNIVERSAL QUANTUM FLUCTUATIONS

Classical evolution of expectation values reflects ergodization. Namely, fluctuations are completely smoothed away if we wait long enough. As opposed to that, quantum fluctuations persist and are not smoothed away. This means that quantum mechanically the quasistatic limit does not exist. At any moment the state of the system cannot be regarded as stationary. In Fig. 12 of Appendix F we demonstrate the dependence of N_{states} on the waiting time T. The same fluctuations are reflected if we plot N_{states} versus Φ. We reemphasize that such fluctuations are absent in the semiclassical simulations. (Therefore we set $T = 0$ in the semiclassical simulations of Fig. 3.)

VIII. QCC AND ITS BREAKDOWN

We already pointed out that the semiclassical dynamics is reflected in the quantum simulations (see Fig. 3). The term "reflected" does not imply "correspondence." We would like to explain the observed breakdown of QCC for slow sweep.

For an extremely slow sweep (that cannot be realized in practice), the quantum dynamics would follow the ground state. This can be regarded as a *quantum detour* of the classical nonadiabatic arena that was looming ahead. For realistic sweep rate the dynamics follows *diabatically* the metastable minimum. But still the probability can leak to levels that are crossed along the way. This early leakage becomes more probable as the forbidden area shrinks (low energetic barrier), and definitely once it is replaced by dynamical barriers of the Kolmogorov-Arnold-Moser (KAM) type [29,30].

The lifetime τ of the condensate can be extracted from the local density of states (LDOS) of the Hamiltonian (see Appendix J). The interesting range, as explained above, is $\Phi_{\text{stb}} < \Phi < \Phi_{\text{dyn}}$. In this range the classical cloud has a piece that is trapped on a dynamically stable island, and therefore cannot decay. But quantum mechanically the cloud can tunnel through the KAM barriers, and therefore has a finite lifetime $\tau(\Phi)$.

We are now equipped to estimate the border between the various $\dot{\Phi}$ regimes. The quantum adiabatic regime is determined by the standard condition $|d\mathcal{H}/dt| < \kappa^2$, where κ is the tunnel coupling, that determines the level splitting. As discussed earlier this condition is never satisfied in practice due to the smallness of κ. Using $\alpha \equiv |d\mathcal{H}/d\Phi| \sim K$, we can rewrite the adiabatic condition as follows:

$$\tau(\Phi) < \frac{\Delta\Phi}{\dot{\Phi}} \qquad (15)$$

where $\Delta\Phi = \kappa/\alpha$, is the parametric width of the avoided crossing, and $\tau \sim 1/\kappa$ is the time to make a Rabi transition. We can extend this reasoning to Fermi's "golden rule" regime where κ becomes larger than the effective levels spacing Δ_0. The latter refers to the participating levels of the LDOS. There we expect $\tau = 1/\gamma$, with $\gamma = 2\pi\kappa^2/\Delta_0$. The condition for having an escape before Φ_{dyn} is obtained from Eq. (15), and implies a crossover at $\dot{\Phi} \approx 10^{-4}\pi$, in rough agreement with Fig. 4.

IX. DISCUSSION

Considering a closed classical Hamiltonian driven system, such as a particle in a box with moving wall (also known as the piston paradigm), the common claim in statistical mechanics textbooks is that quasistatic processes are adiabatic, with vanishing dissipation, and hence reversible. This statement is indeed established for *integrable* [1] and for fully *chaotic* systems [2–8]. But generic systems are neither integrable nor completely chaotic. Rather they have *mixed phase space*. For such a system the quasistatic limit is not adiabatic [20–24], and therefore we expect irreversibility. This irreversibility can be regarded as the higher-dimensional version of separatrix crossing [9–19], where the so-called Kruskal-Neishtadt-Henrard theorem is followed.

In the present paper we wanted not just to expand the analysis of classical irreversibility, but also to explore the quantized version. We asked whether the distinct mechanisms of classical irreversibility are reflected in the quantum-mechanical arena, and how this reconciles with the observation that quantum dynamics, unlike classical dynamics, is always reversible in the strict quasistatic (adiabatic) limit. Our main observations are as follows.

(1) The TOA, and the associate LZ picture, do not provide a proper framework for the analysis of the depletion process. We need at least three orbitals in order to capture the essential features of the dynamics. This means that we are dealing here with a quantum chaos problem.

(2) The Bogoliubov approximation, unlike the naive TOA, implies a gentle type of irreversibility that is related to relay shuttling, and not to diabatic ejection.

(3) Beyond the Bogoliubov approximation we have a chaos-assisted mechanism that competes with the relay-shuttling process. This mechanism becomes dominant in the deeper quasistatic regime.

(4) Accordingly, with regard to the sweep rate, one has to distinguish between the nonquasistatic regime, relay-shuttling regime, chaos-assisted regime, and quantum adiabatic regime. For a many-body condensate, the latter is not accessible in practice.

(5) Quantum features dominate the quantum adiabatic regime and the chaos-assisted regime. The most prominent effect can be described as a version of universal quantum fluctuations.

(6) In the same regime, breakdown of QCC is conspicuous. It is related to leakage of probability along the diabatic transitions. Such leakage does not exist in the semiclassical simulations.

On the practical side one observes that the optimization of a protocol is related to the crossovers between the various regimes. Sweeping a control parameter "too fast" takes us out of the quasistatic regime, while "too slow" is affected by chaos. UQF possibly can be exploited for fine tuning, whose purpose is to minimize chaos-related irreversibility. In analogy with the claim that diagonalization of the Hamiltonian can provide "one shot" phase-space tomography [73], also here we can say that relatively cheap quantum simulations can provide information on the classical dynamics for a cloud of trajectories.

APPENDIX A: THE BHH FOR THE DIMER

The BHH Eq. (2) for an $L = 2$ dimer is

$$\mathcal{H}_{\text{dimer}} = \sum_{j=0,1} \left[\epsilon_j a_j^\dagger a_j + \frac{U}{2} a_j^\dagger a_j^\dagger a_j a_j \right] \qquad (A1)$$

$$- \frac{K}{2}(a_1^\dagger a_0 + a_0^\dagger a_1). \qquad (A2)$$

In momentum representation (the ground-state orbital labeled as "0" and excited orbital labeled as "+") it takes the form

$$\mathcal{H}_{\text{dimer}} = \sum_{k=0,+} \mathcal{E}_k n_k - \frac{\epsilon}{2}(b_0^\dagger b_+ + b_+^\dagger b_0) + \frac{U}{4}(N-1)N$$

$$+ \frac{U_o}{2} n_+ n_0 + \frac{U_\parallel}{4}(b_+^\dagger b_+^\dagger b_0 b_0 + \text{H.c.}) \qquad (A3)$$

with $\mathcal{E}_k = \mp(K/2)$ and $U_0 = U_\parallel = U$. Making the substitution $b_j \mapsto \sqrt{n_j} e^{i\varphi_j}$, and $n_0 = N-n$, and $n_+ = n$, we get

$$\mathcal{H}_{\text{dimer}} = E_0 + \mathcal{E}n - \epsilon\sqrt{(N-n)n}\cos(\varphi)$$

$$+ \frac{U_o}{2}(N-n)n + \frac{U_\parallel}{2}(N-n)n\cos(2\varphi) \qquad (A4)$$

where $E_0 = N\mathcal{E}_0 + (U/4)(N-1)N$ is a constant that can be dropped, and $\mathcal{E} = \mathcal{E}_+ - \mathcal{E}_0 = K$ is the detuning of the two orbitals.

One can write the interaction term of Eq. (A3) using generators of spin rotations. We define $S_x = (n_+ - n_0)/2$, while $n_+ + n_0 = N$, and use the identity

$$S_\Delta^2 \equiv S_z^2 - S_y^2 = \tfrac{1}{2}(b_+^\dagger b_+^\dagger b_0 b_0 + \text{H.c.}). \qquad (A5)$$

Dropping a constant we get

$$\mathcal{H}_{\text{dimer}} = -\mathcal{E}S_x - \epsilon S_z - \frac{U_o}{2}S_x^2 + \frac{U_\parallel}{2}S_\Delta^2. \qquad (A6)$$

We substitute $S_\Delta^2 = S_z^2 - S_y^2$, and in order to get rid of S_y^2 exploit that $S_x^2 + S_y^2 + S_z^2$ is a constant of motion. Thus the final expression can be written as in Eq. (8), with $U_\perp = (U_\parallel - U_o)/2$.

APPENDIX B: BHH INTERACTION TERM FOR A RING

The momentum index k can be defined mod(L) such that $\bar{k} := (2\pi/L)k$ is the quasimomentum in standard units. For a trimer this index takes the values $k = 0, \pm 1$ or shortly $k = 0, \pm$. The prime in the k summation of Eq. (2) implies that conservation of total momentum is required. The interaction term can be arranged as follows:

$$\frac{1}{2}\sum_k{}' b_{k_1}^\dagger b_{k_2}^\dagger b_{k_3} b_{k_4} = \frac{(N-1)N}{2} + \sum_{\langle k,k'\rangle} n_k n_{k'} + \mathcal{H}^{\text{pairing}}$$
$$+ \mathcal{H}^{\text{scattering}}. \quad \text{(B1)}$$

The second term reflects the cost of fragmentation. The summation is over pairs (without double counting). The last term includes scattering events that involve four different orbitals, while the pairing events involve only three orbitals (two k particles split into $k \pm q$ orbitals, and vice versa). In the special case $L = 3$, the scattering events are absent. Dropping a constant, we are left with

$$\frac{U}{L}\left\{ \sum_{\langle k,k'\rangle} n_k n_{k'} + \sum_{k=0,\pm} (b_{k+1}^\dagger b_{k-1}^\dagger b_k b_k + \text{H.c.}) \right\}. \quad \text{(B2)}$$

The Bogoliubov approximation is obtained if we keep in the second term only the $k = 0$ transitions. Then we get

$$\frac{U}{L}[n_0 n_+ + n_0 n_- + n_+ n_- + n_0\sqrt{n_+ n_-} \times 2\cos(2\varphi)]. \quad \text{(B3)}$$

Using n and M as coordinates this expression takes the form

$$\frac{U}{L}\left[(N-n)n + \frac{1}{4}(n^2 - M^2) \right]$$
$$+ \frac{U}{L}(N-n)\sqrt{n^2 - M^2}\cos(2\varphi). \quad \text{(B4)}$$

Setting $M = 0$, the above terms are formally the same as that of the dimer, provided we allow different coefficients $U_o = (3/(2L))U$ and $U_\parallel = (2/L)U$, and include the term $NU/(4L)$ in Eq. (11). On the other hand, if we keep in Eq. (B3) only the n_0 and the n_+, we get the TOA where $U_o = (2/L)U$ and $U_\parallel = 0$.

For completeness we write the full Hamiltonian, without tilt as $\mathcal{H}^{(0)} + \mathcal{H}^{(+)} + \mathcal{H}^{(-)} + \text{const}$. The integrable part can be written as follows:

$$\mathcal{H}^{(0)} = -\frac{U}{12}M^2 + \mathcal{E}_\perp M + \mathcal{E}n + \frac{U_o}{2}(N-n)n$$
$$+ \frac{U_\parallel}{2}(N-n)\sqrt{n^2 - M^2}\cos(2\varphi) \quad \text{(B5)}$$

where the detuning parameters are

$$\mathcal{E} = \frac{1}{2}(\mathcal{E}_+ + \mathcal{E}_-) - \mathcal{E}_0 + \frac{NU}{4L}, \quad \text{(B6)}$$

$$\mathcal{E}_\perp = \frac{1}{2}(\mathcal{E}_+ - \mathcal{E}_-). \quad \text{(B7)}$$

The non-Bogoliubov terms in the $L = 3$ trimer Hamiltonian arise from interaction that involves pairs that move in or out of excited orbitals. In action angle coordinates the explicit expression for them is

$$\mathcal{H}^{(\pm)} = \frac{U}{3\sqrt{2}}\sqrt{(N-n)(n\pm M)}\,(n\mp M)\cos(3\phi\mp\varphi). \quad \text{(B8)}$$

The non-Bogoliubov terms spoil the integrability of the BHH, and generate chaotic motion in phase space.

APPENDIX C: INDICATORS OF QUANTUM CHAOS

The simplest indicator for quantum chaos is level repulsion. In practice it is useful to define

$$r_n = \frac{\min(\Delta_\nu, \Delta_{\nu+1})}{\max(\Delta_\nu, \Delta_{\nu+1})} \quad \text{(C1)}$$

where $\Delta_\nu = E_{\nu+1} - E_\nu$ is the level spacing. The average of r_n within an energy window is expected to be $\langle r \rangle \approx 0.536$ for Wigner-Dyson (chaotic) statistics, as opposed to $\langle r \rangle \approx 0.386$ for Poissonian (nonergodic) statistics. A possibly better indicator is extracted from the matrix elements of the current operator $I_{\nu,\mu} = \langle \nu | (-\partial\mathcal{H}/\partial\Phi) | \mu \rangle$. The band profile of this matrix is related by Fourier transform to the current-current correlation function, and therefore its area $s_\nu = \sum_{\mu(\neq\nu)} |I_{\nu,\mu}|^2$ reflects the correlation time. A related measure, and discussion of its L dependence, can be found in [72].

APPENDIX D: THE BRANCHING OF THE CLOUD

Figure 9 shows what the evolution of the cloud of Fig. 3 looks like in occupation space, using n, M coordinates. This figure provides an optional view of the branching: one piece of
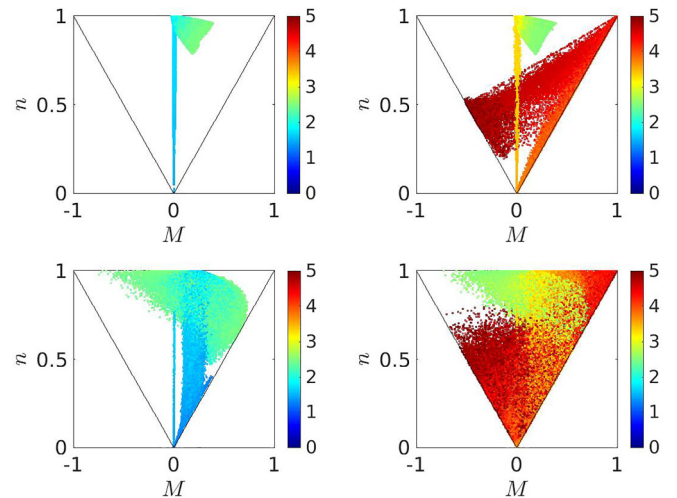

FIG. 9. Evolution of the cloud in occupation space. Optional plots for the semiclassical simulations of Fig. 3. The left and the right panels are for the forward and for the reversed sweep, with the optimal sweep rate $\dot\Phi = 5\pi \times 10^{-4}$ (upper panels), and the very slow (nonoptimal) forward sweep with $\dot\Phi = 5\pi \times 10^{-5}$ (lower panels). The optimal sweep rate has been determined by the minimum of the black curve in Fig. 5(b), meaning that it is slow, but not too slow, such that relay shuttling is still dominant. The color code reflects the time (the initial $t = 0$ cloud is blue, and the final cloud is red).
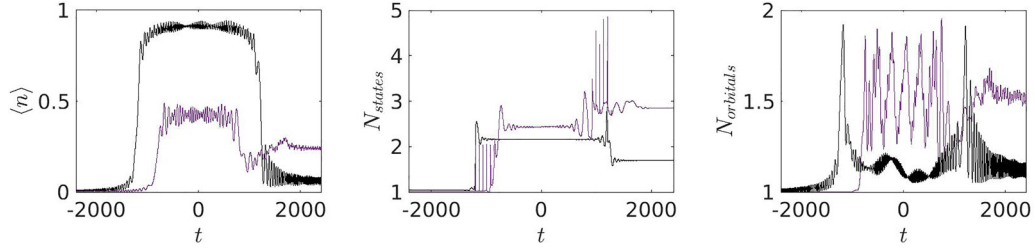
FIG. 10. Depletion vs time for the dimer. The depletion $\langle n \rangle$, and N_{states} and N_{orbitals}, are plotted as a function of time for the diabatic ejection scenario (purple) and for relay shuttling (black). Simulations parameters are as in Fig. 6. There is no relation between the two scenarios: they are combined in one plot for presentation purposes. The only meaningful comparison concerns the question of whether the reversed sweep is capable of restoring the initial state.

the cloud drifts away from $M = 0$ starting at Φ_{stb}, and another piece shuttles along $M = 0$ starting at Φ_{dyn}. The branching is visible only for very slow sweep. In the forward sweep the drift stops after a short duration because the ceiling of the potential is going down, hence blocking further expansion. But in the reversed sweep the ceiling of the potential is going up, and therefore the branching becomes conspicuous.

APPENDIX E: PARTICIPATING ORBITALS

The one-particle reduced probability matrix that is associated with a many-body state is $\rho_{k',k} = (1/N)\langle b_k^\dagger b_{k'} \rangle$. We define

$$N_{\text{orbitals}} = [\text{Tr}(\rho^2)]^{-1}. \quad \text{(E1)}$$

This is a measure for fragmentation. For a many-body coherent state $N_{\text{orbitals}} = 1$, meaning that all the particles are condensed in a single orbital. Semiclassically, such state can be pictured as a localized Gaussian-like distribution in phase space. It is important to realize that at the end of a relay-shuttling process we get $N_{\text{orbitals}} = 1$ in the reduced dimer representation, but $N_{\text{orbitals}} = 2$ in the proper trimer representation, reflecting a twin Fock state (half of the particles in each orbital). At the swap we have $N_{\text{orbitals}} = 3$. Appendix F provides plots of $N_{\text{orbitals}}(t)$ and $N_{\text{states}}(t)$ for the protocols that are discussed in the main text.

For a dimer, the $N_{\text{orbitals}} = 1$ coherent states are related as follows to the Fock states $|n\rangle$:

$$|\theta, \varphi\rangle = \sum_{n=0}^{N} \sqrt{\binom{N}{n}} \left[\cos\frac{\theta}{2}\right]^{N-n} \left[\sin\frac{\theta}{2}\right]^n e^{in\varphi} |n\rangle. \quad \text{(E2)}$$
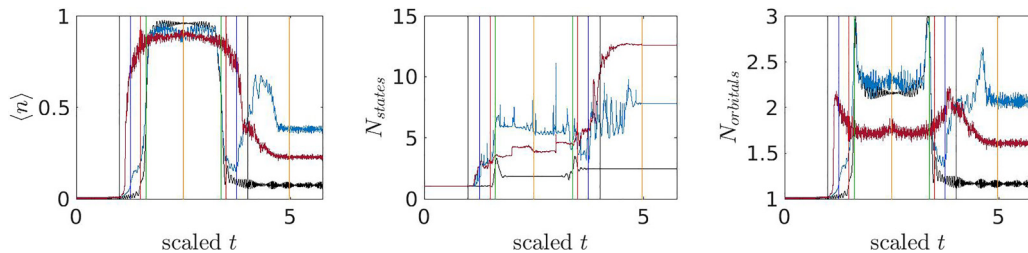
The Husimi function uses this overcomplete basis in order to represent the many-body quantum state on the (S_x, S_y, S_z) Bloch sphere. Namely, it is defined as follows:

$$Q(\theta, \varphi) = |\langle \theta, \varphi | \psi \rangle|^2. \quad \text{(E3)}$$

If $n = (N/2) - S_z$ were the occupation coordinate in the position (site) basis, then $\theta = 0$ would be located at the north pole. But we have defined $n = (N/2) - S_x$ as the occupation coordinate in the momentum (orbital) basis. Therefore our $n = 0$ is located at the east pole, which is redefined as the origin for θ. Accordingly $S_x = (N/2)\cos(\theta)$. We plot images of the Husimi function using (S_x, S_z) coordinates.

APPENDIX F: DEPLETION AND SPREADING AS A FUNCTION OF TIME

We present figures that provide examples for the temporal variation of $\langle n \rangle$ and N_{states} and N_{orbitals}. Figure 10 is for the dimer simulations, while Figs. 11 and 12 are for the trimer. Figure 10 demonstrates that relay shuttling is rather reversible. As opposed to that, in diabatic ejection we have splitting in the reversed sweep, which is reflected in N_{states} and N_{orbitals}, and also spoils $\langle n \rangle$. In Fig. 11 we include a black line that is generated by the Bogoliubov-approximated Hamiltonian $\mathcal{H}^{(0)}$. This approximation is formally equivalent to the relay-shuttling scenario of Fig. 10. Note that its t_d agrees with the blue line, but not with the red line (very slow sweep), reflecting that different depletion scenarios are involved.

APPENDIX G: TOA VS Bogoliubov

As far as U is concerned, naive TOA for any ring ($L > 2$) gives no hopping. Therefore TOA implies that $\mathcal{H}$ of the rings
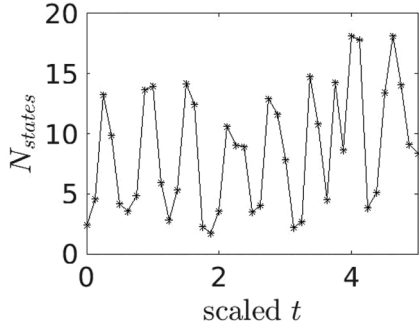

FIG. 11. Depletion vs time for the trimer. The depletion $\langle n \rangle$, and N_{states} and N_{orbitals}, are plotted as a function of time for $\dot{\Phi} = 5\pi \times 10^{-4}$ (blue) and for very slow rate $\dot{\Phi} = 3.33\pi \times 10^{-7}$ (red). The black line is generated with the Bogoliubov-approximated Hamiltonian $\mathcal{H}^{(0)}$ for $\dot{\Phi} = 5\pi \times 10^{-4}$. The other model parameters and the vertical lines are as in Fig. 3.

FIG. 12. Irreversibility vs waiting time. This is an additional panel for Fig. 5. It illustrates the erratic dependence of N_{states} on the waiting time for $\dot{\Phi} = 5\pi \times 10^{-6}$. In the main-text figure a few values of N_{states} are sampled for each $\dot{\Phi}$.

takes the form of the dimer Hamiltonian Eq. (A3) without the last term. We can compare it to the approximation that [69] is using for a continuous ring of length $2\pi R \equiv La$. To get this limit the lattice constant a should be taken to zero, keeping La constant. In this limit $K = (ma^2)^{-1}$ is related to the mass of the particle. The gauge field is $\Phi = (\pi R^2) \times 2m\Omega$, where Ω is the rotation frequency. The single-particle energies are

$$\mathcal{E}_k = \frac{1}{2mR^2}(k - m\Omega R^2)^2, \qquad k = \text{integer}. \tag{G1}$$

Hence, up to a constant, $\mathcal{E}$ is identified as the rotation frequency:

$$\mathcal{E} = \mathcal{E}_1 - \mathcal{E}_0 = \frac{1}{2mR^2} - \Omega. \tag{G2}$$

One wonders whether the discussion of "Nucleation in finite topological systems during continuous metastable quantum phase transitions" [69] is flawed. In order to answer this question we have to appreciate the physical significance of the continuum limit $L \to \infty$ that was considered there. It is physically clear that "rotation" of a flat clean ring (that has neither tilt nor lattice potential) is an empty notion: nothing changes in the Hamiltonian. Furthermore, in this limit, chaos is not an issue (the $L \to \infty$ limit is integrable). The physics that we discuss becomes relevant as L becomes finite, and irreversibility is most pronounced for $L = 3$.

Still one may insist on adopting TOA for a finite L ring. How would the results be in comparison with the correct picture? Looking at Fig. 3 of [69] we see that the interest there is in simple adiabatic shuttling along the upper level, during which no bifurcation occurs. In this energy range there is no major difference between the TOA and the Bogoliubov versions, as we see from looking on the higher levels in Fig. 6. But for the scenario that we consider, starting at $n = 0$, the TOA completely fails. Demonstration of this colossal failure is provided in Fig. 13.

APPENDIX H: SIMULATIONS WITH A TILTED RING

Figure 13 compares the dynamics that is generated by $\mathcal{H}$ with the dynamics that is generated using TOA. In the TOA Hamiltonian we keep just two momentum orbitals. Without tilt the TOA Hamiltonian is identical with the $U = 0$ Hamiltonian, and therefore its failure is trivial (not displayed). We
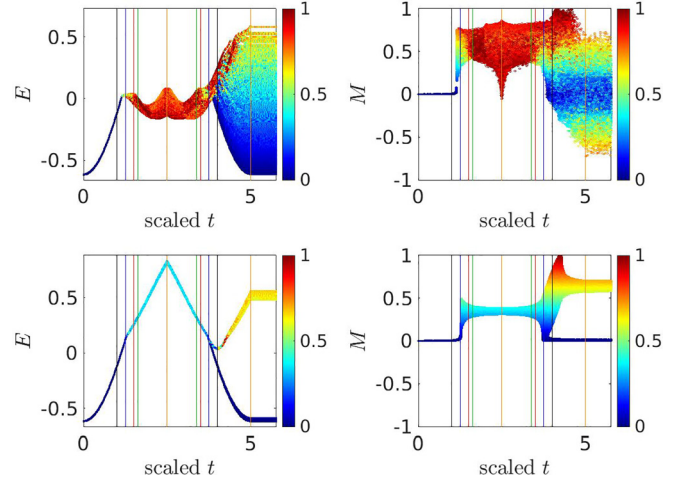

FIG. 13. Simulations with a tilted ring. These are additional panels for Fig. 3 of the main text. The parameters are the same as for the left panels there ($\dot{\Phi} = 5\pi \times 10^{-4}$), with added tilt $\epsilon = 0.1$. The upper panels are generated with the full Hamiltonian, while the lower panels use TOA.

therefore add a tilt $\epsilon \neq 0$ as in [69]. We see that the TOA completely fails to reproduce the dynamics.

APPENDIX I: BIFURCATIONS

The (S_x, S_z) contour lines of the Hamiltonian Eq. (8) are ellipses that are chopped by the circle $S_x^2 + S_z^2 = (N/2)^2$. If the circle is ignored, the minimum is at

$$(S_x, S_z) = \left(\frac{\mathcal{E}}{2U_\perp}, \frac{\epsilon}{2U_\parallel} \right). \tag{I1}$$

In the relay-shuttling scenario, as $\mathcal{E}$ is varied, a bifurcation takes place at the east pole once this minimum enters into the circle. This happens at Eq. (13). In the adiabatic ejection scenario the relevant bifurcation happens on the bounding circle: before the bifurcation we have on the circle one minimum and one maximum; after the bifurcation a secondary minimum and an associated saddle point appear. In order to find the bifurcation we define the function

$$h(\theta) = H\left(S_x := \frac{N}{2}\cos(\theta), S_z := \frac{N}{2}\sin(\theta) \right). \tag{I2}$$

Then we write the equations $h'(\theta) = 0$ and $h''(\theta) = 0$, for the first and second derivatives, as required at the bifurcation point. The combined equations $\sin\theta \, h''(\theta) - \cos\theta \, h'(\theta) = 0$ and $\cos\theta \, h''(\theta) + \sin\theta \, h'(\theta) = 0$ are solved to get Eq. (12).

APPENDIX J: QUANTUM STABILITY OF THE CONDENSATE

For a frozen value of Φ we perform simulations whose purpose is to monitor the stability of the quantum condensate. The interest is in the regime $\Phi_{\text{stb}} < \Phi < \Phi_{\text{dyn}}$. In this regime the classical cloud has a piece that is trapped on a dynamically stable island, and therefore cannot decay. But quantum mechanically the cloud can tunnel through the KAM barriers, and therefore has a finite lifetime τ. The survival probability

$P(t) = |\langle\Psi(0)|\Psi(t)\rangle|^2$ of the condensate has been found for representative values of Φ. From that τ has been extracted. In the range of interest, for our choice of parameters, $\tau \approx 90$.

The survival amplitude is related to the LDOS via a Fourier transform, and therefore one can say that we employ here an LDOS based determination of τ.

[1] L. D. Landau and E. M. Lifshitz, *Mechanics*, 3rd. ed. (Elsevier, Amsterdam, 1982), p. 154ff.

[2] E. Ott, Goodness of Ergodic Adiabatic Invariants, Phys. Rev. Lett. **42**, 1628 (1979).

[3] R. Brown, E. Ott, and C. Grebogi, Ergodic Adiabatic Invariants of Chaotic Systems, Phys. Rev. Lett. **59**, 1173 (1987).

[4] R. Brown, E. Ott, and C. Grebogi, The goodness of ergodic adiabatic invariants, J. Stat. Phys. **49**, 511 (1987).

[5] M. Wilkinson, A semiclassical sum rule for matrix elements of classically chaotic systems, J. Phys. A: Math. Gen. **20**, 2415 (1987).

[6] M. Wilkinson, Statistical aspects of dissipation by Landau-Zener transitions, J. Phys. A: Math. Gen. **21**, 4021 (1988).

[7] D. Cohen, Quantum Dissipation due to the Interaction with Chaotic Degrees of Freedom and the Correspondence Principle, Phys. Rev. Lett. **82**, 4951 (1999).

[8] D. Cohen, Chaos and energy spreading for time-dependent Hamiltonians, and the various regimes in the theory of quantum dissipation, Ann. Phys. (NY) **283**, 175 (2000).

[9] D. Dobbrott and J. M. Greene, Probability of trapping-state transition in a toroidal device, Phys. Fluids **14**, 1525 (1971).

[10] A. I. Neishtadt, Passage through a separatrix in a resonance problem with a slowly-varying parameter, J. Appl. Math. Mech. **39**, 594 (1975).

[11] A. V. Timofeev, On the constancy of an adiabatic invariant when the nature of the motion changes, Sov. Phys. JETP **48**, 656 (1978).

[12] J. Henrard, Capture into resonance: An extension of the use of adiabatic invariants, Celestial Mech. **27**, 3 (1982).

[13] J. R. Cary, D. F. Escande, and J. L. Tennyson, Adiabatic-invariant change due to separatrix crossing, Phys. Rev. A **34**, 4256 (1986).

[14] J. H. Hannay, Accuracy loss of action invariance in adiabatic change of a one-freedom Hamiltonian, J. Phys. A: Math. Gen. **19**, L1067 (1986).

[15] J. R. Cary and R. T. Skodje, Reaction Probability for Sequential Separatrix Crossings, Phys. Rev. Lett. **61**, 1795 (1988).

[16] A. I. Neishtadt, Probability phenomena due to separatrix crossing, Chaos **1**, 42 (1991).

[17] Y. Elskens and D. F. Escande, Slowly pulsating separatrices sweep homoclinic tangles where islands must be small: An extension of classical adiabatic theory, Nonlinearity **4**, 615 (1991).

[18] T. Eichmann, E. P. Thesing, and J. R. Anglin, Engineering separatrix volume as a control technique for dynamical transitions, Phys. Rev. E **98**, 052216 (2018).

[19] A. Neishtadt, On mechanisms of destruction of adiabatic invariance in slow-fast Hamiltonian systems, Nonlinearity **32**, R53 (2019).

[20] V. Gelfreich, V. Rom-Kedar, and D. Turaev, Oscillating mushrooms: Adiabatic theory for a non-ergodic system, J. Phys. A: Math. Theor. **47**, 395101 (2014).

[21] K. Shah, D. Turaev, V. Gelfreich, and V. Rom-Kedar, Equilibration of energy in slow-fast systems, Proc. Natl. Acad. Sci. USA **114**, E10514 (2017).

[22] A. Dey, D. Cohen, and A. Vardi, Adiabatic Passage through Chaos, Phys. Rev. Lett. **121**, 250405 (2018).

[23] R. Bürkle, A. Vardi, D. Cohen, and J. R. Anglin, Probabilistic Hysteresis in Integrable and Chaotic Isolated Hamiltonian Systems, Phys. Rev. Lett. **123**, 114101 (2019).

[24] Y. Winsten and D. Cohen, Quasistatic transfer protocols for atomtronic superfluid circuits, Sci. Rep. **11**, 3136 (2021).

[25] J. Liu, L.-B. Fu, B.-Y. Ou, S.-G. Chen, and Q. Niu, Theory of nonlinear Landau-Zener tunneling, Phys. Rev. A **66**, 023404 (2002).

[26] B. Wu and Q. Niu, Nonlinear Landau-Zener tunneling, Phys. Rev. A **61**, 023402 (2000).

[27] K. Smith-Mannschott, M. Chuchem, M. Hiller, T. Kottos, and D. Cohen, Occupation Statistics of a BEC for a Driven Landau-Zener Crossing, Phys. Rev. Lett. **102**, 230401 (2009).

[28] G. Kalosakas, A. R. Bishop, and V. M. Kenkre, Multiple-timescale quantum dynamics of many interacting bosons in a dimer, J. Phys. B: At. Mol. Opt. Phys. **36**, 3233 (2003).

[29] T. Geisel, G. Radons, and J. Rubner, Kolmogorov-Arnol'd-Moser Barriers in the Quantum Dynamics of Chaotic Systems, Phys. Rev. Lett. **57**, 2883 (1986).

[30] N. T. Maitra and E. J. Heller, Quantum transport through cantori, Phys. Rev. E **61**, 3620 (2000).

[31] A. Dey, D. Cohen, and A. Vardi, Many-body adiabatic passage: Quantum detours around chaos, Phys. Rev. A **99**, 033623 (2019).

[32] L. Amico *et al.*, Roadmap on atomtronics: State of the art and perspective, AVS Quantum Sci. **3**, 039201 (2021).

[33] M. Albiez, R. Gati, J. Folling, S. Hunsmann, M. Cristiani, and M. K. Oberthaler, Direct Observation of Tunneling and Nonlinear Self-Trapping in a Single Bosonic Josephson Junction, Phys. Rev. Lett. **95**, 010402 (2005).

[34] S. Levy, E. Lahoud, I. Shomroni, and J. Steinhauer, The ac and dc Josephson effects in a Bose-Einstein condensate, Nature (London) **449**, 579 (2007).

[35] O. Morsch and M. Oberthaler, Dynamics of Bose-Einstein condensates in optical lattices, Rev. Mod. Phys. **78**, 179 (2006).

[36] I. Bloch, J. Dalibard, and W. Zwerger, Many-body physics with ultracold gases, Rev. Mod. Phys. **80**, 885 (2008).

[37] L. Amico, D. Aghamalyan, F. Auksztol, H. Crepaz, R. Dumke, and L. C. Kwek, Superfluid qubit systems with ring shaped optical lattices, Sci. Rep. **4**, 4298 (2014).

[38] G.-S. Paraoanu, Persistent currents in a circular array of Bose-Einstein condensates, Phys. Rev. A **67**, 023607 (2003).

[39] D. W. Hallwood, K. Burnett, and J. Dunningham, Macroscopic superpositions of superfluid flows, New J. Phys. **8**, 180 (2006).

[40] G. Arwas and D. Cohen, Chaos and two-level dynamics of the atomtronic quantum interference device, New J. Phys. **18**, 015007 (2016).

[41] J. C. Eilbeck, P. S. Lomdahl, and A. C. Scott, The discrete self-trapping equation, Physica D **16**, 318 (1985).

[42] D. Hennig, H. Gabriel, M. F. Jorgensen, P. L. Christiansen, and C. B. Clausen, Homoclinic chaos in the discrete self-trapping trimer, Phys. Rev. E **51**, 2870 (1995).

[43] S. Flach and V. Fleurov, Tunnelling in the nonintegrable trimer: A step towards quantum breathers, J. Phys.: Condens. Matter **9**, 7039 (1997).

[44] K. Nemoto, C. A. Holmes, G. J. Milburn, and W. J. Munro, Quantum dynamics of three coupled atomic Bose-Einstein condensates, Phys. Rev. A **63**, 013604 (2000).

[45] R. Franzosi and V. Penna, Chaotic behavior, collective modes, and self-trapping in the dynamics of three coupled Bose-Einstein condensates, Phys. Rev. E **67**, 046227 (2003).

[46] M. Johansson, Hamiltonian Hopf bifurcations in the discrete nonlinear Schrödinger trimer: Oscillatory instabilities, quasiperiodic solutions and a new type of self-trapping transition, J. Phys. A: Math. Gen. **37**, 2201 (2004).

[47] M. Hiller, T. Kottos, and T. Geisel, Complexity in parametric Bose-Hubbard Hamiltonians and structural analysis of eigenstates, Phys. Rev. A **73**, 061604(R) (2006).

[48] C. Lee, T. J. Alexander, and Y. S. Kivshar, Melting of Discrete Vortices via Quantum Fluctuations, Phys. Rev. Lett. **97**, 180408 (2006).

[49] E. M. Graefe, H. J. Korsch, and D. Witthaut, Mean-field dynamics of a Bose-Einstein condensate in a time-dependent triple-well trap: Nonlinear eigenstates, Landau-Zener models, and stimulated Raman adiabatic passage, Phys. Rev. A **73**, 013617 (2006).

[50] A. R. Kolovsky, Semiclassical Quantization of the Bogoliubov Spectrum, Phys. Rev. Lett. **99**, 020401 (2007).

[51] P. Buonsante, V. Penna, and A. Vezzani, Quantum signatures of the self-trapping transition in attractive lattice bosons, Phys. Rev. A **82**, 043615 (2010).

[52] T. F. Viscondi and K. Furuya, Dynamics of a Bose–Einstein condensate in a symmetric triple-well trap, J. Phys. A: Math. Theor. **44**, 175301 (2011).

[53] P. Jason, M. Johansson, and K. Kirr, Quantum signatures of an oscillatory instability in the Bose-Hubbard trimer, Phys. Rev. E **86**, 016214 (2012).

[54] L. Morales-Molina, S. A. Reyes, and M. Orszag, Current and entanglement in a three-site Bose-Hubbard ring, Phys. Rev. A **86**, 033629 (2012).

[55] A. Gallemí, M. Guilleumas, J. Martorell, R. Mayol, A. Polls, and B. Juliá-Díaz, Fragmented condensation in Bose-Hubbard trimers with tunable tunnelling, New J. Phys. **17**, 073014 (2015).

[56] G. Arwas, A. Vardi, and D. Cohen, Triangular Bose-Hubbard trimer as a minimal model for a superfluid circuit, Phys. Rev. A **89**, 013601 (2014).

[57] G. Arwas, A. Vardi, and D. Cohen, Superfluidity and chaos in low dimensional circuits, Sci. Rep. **5**, 13433 (2015).

[58] G. Arwas and D. Cohen, Superfluidity in Bose-Hubbard circuits, Phys. Rev. B **95**, 054505 (2017).

[59] G. Arwas and D. Cohen, Monodromy and chaos for condensed bosons in optical lattices, Phys. Rev. A **99**, 023625 (2019).

[60] A. R. Kolovsky, Bose-Hubbard Hamiltonian: Quantum chaos approach, Int. J. Mod. Phys. B **30**, 1630009 (2016).

[61] A. Trenkwalder, G. Spagnolli, G. Semeghini, S. Coop, M. Landini, P. Castilho, L. Pezzè, G. Modugno, M. Inguscio, A. Smerzi, and M. Fattori, Quantum phase transitions with parity-symmetry breaking and hysteresis, Nat. Phys. **12**, 826 (2016).

[62] A. L. Fetter, Rotating trapped Bose-Einstein condensates, Rev. Mod. Phys. **81**, 647 (2009).

[63] S. Eckel, J. G. Lee, F. Jendrzejewski, N. Murray, C. W. Clark, C. J. Lobb, W. D. Phillips, M. Edwards, and G. K. Campbell, Hysteresis in a quantized superfluid "atomtronic" circuit, Nature (London) **506**, 200 (2014).

[64] C. Ryu, P. W. Blackburn, A. A. Blinova, and M. G. Boshier, Experimental Realization of Josephson Junctions for an Atom SQUID, Phys. Rev. Lett. **111**, 205301 (2013).

[65] C. Ryu, E. C. Samson, and M. G. Boshier, Quantum interference of currents in an atomtronic SQUID, Nat. Commun. **11**, 3338 (2020).

[66] E. J. Mueller, Superfluidity and mean-field energy loops: Hysteretic behavior in Bose-Einstein condensates, Phys. Rev. A **66**, 063603 (2002).

[67] B. Wu and Q. Niu, Superfluidity of Bose–Einstein condensate in an optical lattice: Landau–Zener tunnelling and dynamical instability, New J. Phys. **5**, 104 (2003).

[68] M. Machholm, C. J. Pethick, and H. Smith, Band structure, elementary excitations, and stability of a Bose-Einstein condensate in a periodic potential, Phys. Rev. A **67**, 053613 (2003).

[69] O. Fialko, M.-C. Delattre, J. Brand, and A. R. Kolovsky, Nucleation in Finite Topological Systems During Continuous Metastable Quantum Phase Transitions, Phys. Rev. Lett. **108**, 250402 (2012).

[70] S. Baharian and G. Baym, Bose-Einstein condensates in toroidal traps: Instabilities, swallow-tail loops, and self-trapping, Phys. Rev. A **87**, 013619 (2013).

[71] C. Khripkov, A. Vardi, and D. Cohen, Many body dynamical localization and thermalization, Phys. Rev. A **101**, 043603 (2020).

[72] M. Pandey, P. W. Claeys, D. K. Campbell, A. Polkovnikov, and D. Sels, Adiabatic Eigenstate Deformations as a Sensitive Probe for Quantum Chaos, Phys. Rev. X **10**, 041017 (2020).

[73] C. Khripkov, D. Cohen, and A. Vardi, Temporal fluctuations in the bosonic Josephson junction as a probe for phase space tomography, J. Phys. A: Math. Theor. **46**, 165304 (2013).